

Age, metallicity and star formation history of spheroidal galaxies in cluster at $z \sim 1.2$

P. Saracco^{1*}, F. La Barbera², A. Gargiulo³, F. Mannucci⁴, D. Marchesini⁵,
M. Nonino⁶, P. Ciliegi⁷

¹INAF - Osservatorio Astronomico di Brera, via Brera 28, 20121 Milano, Italy

²INAF - Osservatorio Astronomico di Capodimonte, sal. Moiarriello 16, 80131 Napoli, Italy

³INAF - Istituto di Astrofisica e Fisica Cosmica, IASF, via E. Bassini 15, 20133 Milano, Italy

⁴INAF - Osservatorio Astrofisico di Arcetri, Largo Enrico Fermi 5, 50125 Firenze, Italy

⁵Tufts University, Physics and Astronomy Department, 574 Boston Ave, Medford, 02155 MA, USA

⁶INAF - Osservatorio Astronomico di Trieste, Via G.B. Tiepolo 11, 34143 Trieste, Italy

⁷INAF - Osservatorio Astronomico di Bologna, Via Piero Gobetti, 93/3, 40129 Bologna, Italy

Accepted 2018 December 17. Received 2018 November 10; in original form 2018 September 11

ABSTRACT

We present the analysis, based on spectra collected at the *Large Binocular Telescope*, of the stellar populations in seven spheroidal galaxies in the cluster XLSSJ0223 at $z \sim 1.22$. The aim is to constrain the epoch of their formation and their star formation history. Using absorption line strengths and full spectral fitting, we derive for the stellar populations of the seven spheroids a median age $\langle \text{Age} \rangle = 2.4 \pm 0.6$ Gyr, corresponding to a median formation redshift $\langle z_f \rangle \sim 2.6^{+0.7}_{-0.5}$ (lookback time = $11^{+0.6}_{-1.0}$ Gyr). We find a significant scatter in age, showing that massive spheroids, at least in our targeted cluster, are not coeval. The median metallicity is $[Z/H] = 0.09 \pm 0.16$, as for early-types in clusters at $0 < z < 0.9$. This lack of evolution of $[Z/H]$ over the range $0 < z < 1.3$, corresponding to the last 9 billions years, suggests that no significant additional star formation and chemical enrichment are required for cluster spheroids to reach the present-day population. We do not detect significant correlation between age and velocity dispersion σ_e , or dynamical mass M_{dyn} , or effective stellar mass density Σ_e . On the contrary, the metallicity $[Z/H]$ of the seven spheroids is correlated to their dynamical mass M_{dyn} , according to a relation similar to the one for local spheroids. $[Z/H]$ is also anticorrelated to stellar mass density Σ_e because of the anticorrelation between M_{dyn} and Σ_e . Therefore, the basic trends observed in the local universe were already established at $z \sim 1.3$, i.e. more massive spheroids are more metal rich, have lower stellar mass density and tend to be older than lower-mass galaxies.

Key words: galaxies: evolution; galaxies: elliptical and lenticular, cD; galaxies: formation; galaxies: high redshift

1 INTRODUCTION

The mechanisms through which massive (stellar mass $M_* \approx 10^{11} M_\odot$) spheroidal galaxies assemble and shape their stellar mass and then quench their star formation are still unclear and represent central topics in galaxy evolution. Linking the population of galaxies at different redshifts to constrain their evolution, it is not always a reliable technique, since it is affected by the well known progenitor bias problem (e.g. van Dokkum & Franx 2001; Carollo et al. 2013). The study of spheroids, compared to other types of galaxies, is potentially less affected by this bias, as once

an high-density bulge is formed, it is unlikely that it is disrupted, or assembles efficiently a surrounding disc (e.g. Brooks & Christensen 2016). Therefore, even if not all the local spheroidal galaxies may have a spheroid as progenitor, high-redshift spheroidal galaxies are most probably the progenitors of some of the local ones.

Simulations suggest that an early intense burst of star formation followed by quenching, is required to reproduce the detailed structural properties of ellipticals and to match the observed tight scaling relations (Ciotti et al. 2007; Naab et al. 2007; Oser et al. 2012; Porter et al. 2014; Brooks & Christensen 2016). Observations show that only a minor fraction of local spheroids has accreted newly stellar mass through secondary events of star formation (e.g.

* E-mail: paolo.saracco@inaf.it

Thomas et al. 2010; Gargiulo et al. 2016). Therefore, the stellar populations of high-redshift spheroidal galaxies keep the information of the early-phases of their formation. If their evolution is mostly characterized by passive ageing, then their stellar population properties hold on nearly unchanged till now. Consequently, stellar chemical composition and age are powerful tools to link spheroids across time and, most importantly, to constrain their formation and their past evolution.

Correlations between stellar population parameters and structural parameters of early-type galaxies have been extensively studied in the past. The line strengths of early-type galaxies in the optical spectral range are found to be correlated or anticorrelated to the velocity dispersion, depending whether the lines are more sensitive to metallicity or age effects (e.g. Bender et al. 1993; Fisher et al. 1995; Colless et al. 1999; Jørgensen 1999; Trager et al. 2000; Bernardi et al. 2003, 2006; Harrison et al. 2011; McDermid et al. 2015; Jørgensen et al. 2017). These relationships are observed both for field and cluster early-type galaxies in the local universe and it seems that environment does not affect them significantly (e.g. Bernardi et al. 2006; McDermid et al. 2015). For cluster early-types these relations are observed and well defined up to $z \sim 0.9$ (Jørgensen et al. 2017).

Given the dependence of line-strengths on metallicity and age, it is expected a correlation between age, metallicity and velocity dispersion. Indeed, the metallicity $[Z/H]$ of local spheroidal galaxies, typically solar or super-solar (e.g. Buzzoni et al. 1992; Jørgensen 1999; Thomas et al. 2005), is found to correlate with central velocity dispersion (Greggio 1997; Jørgensen 1999; Trager et al. 2000; Thomas et al. 2005, 2010; Harrison et al. 2011; McDermid et al. 2015). Contrary to metallicity, the correlation between age and velocity dispersion is much less evident and it is more uncertain. Some authors find weak but significant correlation, with older galaxies characterized by higher velocity dispersions (e.g. Thomas et al. 2005; Gallazzi et al. 2005, 2014; Harrison et al. 2011; McDermid et al. 2015). Other authors, find shallower correlations and slopes consistent with zero (e.g. Trager et al. 2000; Jørgensen et al. 2017), especially when age is estimated over an aperture large enough to enclose most of the galaxy light (La Barbera et al. 2010b). Overall, considering velocity dispersion a proxy of galaxy mass, the above relations suggest that more massive galaxies are more metal rich and, possibly, older than their lower mass counterparts.

Actually, the mass-age and the mass-metallicity relations are observed (e.g. Thomas et al. 2010; Gallazzi et al. 2014; McDermid et al. 2015) and both appear well defined when dynamical mass is considered, with the slope of the mass-age relation being rather flat. Thus, most massive early-type galaxies in the local universe are also the most metal rich, which appears counter-intuitive if they are also the oldest (Greggio & Renzini 2011). However, this could be explained by a deep gravitational potential (i.e. a large dark matter halo) that, on one hand, modulates an intense star formation and, on the other hand, efficiently retains the metals rapidly produced by high-mass stars. Another possibility is that, metal rich stars are added later to the stellar population through later episodes of star formation.

Whether and which of the above scenarios is the right

one can be assessed by studying the stellar population properties of high mass spheroids in the past, by establishing whether the relations between stellar population properties and physical and dynamical properties were already in place early on in the evolution of spheroids or not, and whether the local age-velocity dispersion and age-mass relations hold on at high-redshift once evolved back in time.

To investigate these issues, we have performed new spectroscopic observations for 14 spheroids candidate members of the cluster XLSSJ0223-0436 at $z \sim 1.22$. The whole data set will be presented in a forthcoming paper. Here, we present the analysis of the seven spheroids whose spectra have S/N high enough to allow for the study of their stellar population properties. The paper is organized as follows. Section 2 briefly describes the sample, the observations and the data reduction. Section 3 describes the measurement of redshift and absorption line indices. In Section 4, we describe the constraints obtained from absorption line strengths on age and metallicity of the seven spheroids. In Section 5 we make use of full spectral fitting to derive age and metallicity of the galaxy stellar populations and to constrain their star formation histories (SFHs). In Section 6 we study the relationships of age and metallicity with physical and structural parameters, velocity dispersion, dynamical mass and stellar mass density. Section 7 presents a summary of results and conclusions.

Throughout this paper we use a cosmology with $H_0 = 70 \text{ Km s}^{-1} \text{ Mpc}^{-1}$, $\Omega_m = 0.3$, and $\Omega_\Lambda = 0.7$. All the magnitudes are in the Vega system, unless otherwise specified.

2 SPECTROSCOPIC OBSERVATIONS AND DATA REDUCTION

The seven spheroidal galaxies belong to a sample of 23 spheroids candidate cluster members, photometrically selected in the field around the cluster XLSSJ0223-0436 at $z = 1.22$ (Andreon et al. 2005; Bremer et al. 2006). Briefly, the target galaxies were selected among all the galaxies brighter than $z_{850} < 24$ within a projected radius $D \leq 1 \text{ Mpc}$ from the cluster centre. Then, according to their $i_{775} - z_{850}$ colour, galaxies were selected within $\pm 0.2 \text{ mag}$ from the peak of the color distribution centered at the color of the brightest cluster members. Finally, a visual classification on the F850LP images was used to select only those galaxies with elliptical/spheroidal morphology. A detailed description of the whole sample, the structural parameters of galaxies and their scaling relations are given in Saracco et al. (2017).

Spectroscopic observations of the targets were performed in multi-object spectroscopic mode (MOS) with the Multi-Object Double Spectrograph (MODS, 1 and 2) (Pogge et al. 2010) mounted at the Large Binocular Telescope (LBT). Observations confirmed 13 spheroidal galaxies members of the cluster XLSSJ0223. The whole spectroscopic data will be presented in a forthcoming paper (Saracco et al. 2018, in preparation). Here, we focus the analysis on the seven spheroids having the highest S/N, suited to stellar population study.

Observations were carried out with filter GG495 coupled with the grism G670L sampling the wavelength range $0.5 \mu\text{m} < \lambda < 1.0 \mu\text{m}$ at 0.85 \AA/pix . We adopted a slit width of $1.2''$ resulting in a spectral resolution $R \simeq 1150$, corre-

Table 1. List of observed galaxies in the XLSSJ0223 field and spectroscopic redshift measurements.

| ID | RA (h:m:s) | Dec (d:p:s) | F850LP (mag) | $i_{775} - z_{850}$ (mag) | $\log \mathcal{M}_*$ (M_\odot) | $\log \mathcal{M}_{dyn}$ (M_\odot) | z_{spec} | Em ^a | F([OII]) ^b ($\text{erg cm}^{-2} \text{s}^{-1}$) | SFR ($M_\odot \text{yr}^{-1}$) | S/N ^c |
|------|---------------|----------------|------------------|------------------------------|---------------------------------------|---|------------|-----------------|---|-------------------------------------|------------------|
| 651 | 02:23:05.759 | -04:36:10.27 | 21.62 \pm 0.01 | 1.09 \pm 0.02 | 10.94 | 11.29 | 1.2192 | [NeV] | 6 \pm 2 | 0.7 \pm 0.2 | 11.3 |
| 972 | 02:23:04.718 | -04:36:13.47 | 22.61 \pm 0.03 | 0.92 \pm 0.03 | 10.54 | 11.32 | 1.2153 | ... | <6 | <0.8 | 6.2 |
| 1142 | 02:23:03.262 | -04:36:14.60 | 21.30 \pm 0.01 | 1.00 \pm 0.02 | 11.50 | 11.68 | 1.2204 | ... | <1.5 | <0.2 | 12.7 |
| 1370 | 02:23:02.021 | -04:36:43.26 | 23.10 \pm 0.03 | 0.96 \pm 0.04 | 10.08 | 10.10 | 1.2249 | ... | <7 | <0.9 | 5.6 |
| 1442 | 02:22:57.980 | -04:36:22.31 | 21.88 \pm 0.01 | 0.91 \pm 0.02 | 10.80 | 10.67 | 1.2250 | [OII] | 27 \pm 4 | 3.0 \pm 0.4 | 11.3 |
| 1630 | 02:23:00.929 | -04:36:50.19 | 21.48 \pm 0.01 | 1.04 \pm 0.02 | 10.75 | 11.18 | 1.2109 | [OII] | 34 \pm 6 | 4.0 \pm 0.6 | 12.2 |
| 1711 | 02:22:59.990 | -04:36:02.53 | 20.92 \pm 0.01 | 1.02 \pm 0.02 | 11.20 | 11.52 | 1.2097 | ... | ... | ... | 18.2 |

^a Emission lines detected: dots - no emission line $>1\sigma$.

^b Flux is in units of $10^{-18} \text{ erg cm}^{-2} \text{ s}^{-1}$.

^c S/N per Ångstrom in the rest-frame of the galaxy, estimated in the interval $\sim 4000\text{--}4150 \text{ Å}$.

sponding to a FWHM $\sim 7.4 \text{ Å}$ at 8500 Å . A bright star was put in a slit to accurately measure the offsets in the observing sequence and perform the correction for telluric absorption lines (see below). Observations, consisting in a sequence of exposures (ABBA) of 900 sec each at dithered positions offset by $\sim 5''$, were collected both with MODS1 and MODS2 for a total effective integration time of 8 hours.

Raw data were first pre-processed by the MODS pipeline that applies correction for bias-subtraction, flat-field (pixel-to-pixel) variation and for optical distortions, providing also the wavelength calibration through the inverse dispersion solution (0.08 Å rms accuracy). Then, standard reduction was performed with IRAF tasks. A first sky-subtraction was applied by subtracting from each frame the following one in the dithering observing sequence. The sky-subtracted frames were aligned to sub-pixel scale using *drizzle* resampling algorithm, and then co-added. The shifts to align the images were estimated using the positions of the peak of the spectrum collapsed along the wavelengths of the bright star present in the masks. Before co-adding, MODS1 and MODS2 2D spectra were corrected for the relative spectral slit flats, obtained using quartz-halogen flat fields taken through the MOS masks, and for the relative sensitivity function. The sensitivity function was derived from the spectrum of the same spectrophotometric standard star obtained with both cameras.

The 1D spectrum of each galaxy was extracted using the Iraf task *apall*. After extraction, an additional residual sky-subtraction was applied to remove sky residuals due to sky intensity variations between subsequent images in the ABBA sequence. To this end, we subtracted from the 1D object spectrum, the 1D spectrum of sky residuals obtained by averaging the pixels above and below the object, along the spatial direction. Finally, we applied the software MOLECFIT (Kausch et al. 2015) to perform telluric absorption correction, by fitting spectral regions of the bright star spectrum with prominent telluric absorption. The resulting telluric absorption model provided by MOLECFIT was applied to correct all galaxy spectra.

3 MEASUREMENT OF REDSHIFT AND ABSORPTION LINE INDICES

3.1 Redshift measurement

Measurements of spectroscopic redshifts and velocity dispersion were performed using stellar absorption features, by fitting the observed spectra with MILES simple stellar population (SSP) models (Vazdekis et al. 2010). These models are primarily based on the MILES (Sánchez-Blázquez et al. 2006; Falcón-Barroso et al. 2011) and Indo-U.S (Valdes et al. 2004) stellar libraries and have a spectral resolution of 2.5 Å (Beifiori et al. 2011), close to the rest-frame resolution ($\sim 3.3 \text{ Å}$) of our spectra. Spectral fitting was performed using the penalized PiXel-Fitting method (pPXF, Cappellari & Emsellem 2004; Cappellari 2017).

Velocity dispersion measurements for the whole set of spectroscopic observations will be presented in a forthcoming paper (Saracco et al. 2018, in preparation). Here, we summarize the method used. For each spectrum, we derived the broadening of its absorption lines, σ_{obs} , by performing spectral fitting in the range $3550\text{--}4200 \text{ Å}$. The galaxy velocity dispersion, σ_* is then derived by correcting the σ_{obs} for the instrumental broadening of $\sim 111 \text{ km/s}$, resulting from the instrumental resolution $R \sim 1150$ (see §2).

The uncertainties on σ_* have been derived by repeating the measurements on 100 simulated spectra obtained by summing to the best-fitting template the 1D sky residuals extracted from the real 2D spectra, randomly shuffled in wavelength. The typical uncertainties are in the range 10%–25%, with the exception of galaxy #1370 affected by a much larger uncertainty because of the low S/N (see Tab. 1). We have tested the robustness of the measurements against the library of template used and the wavelength range considered by repeating the fitting with a set of synthetic stars extracted from the library of Munari et al. (2005) and a set of SSPs of Bruzual & Charlot (2003), and by slightly varying the fitted spectral range. In all the cases, we obtained measurements well within the estimated errors.

The seven spheroidal cluster members here analysed have S/N $\sim 5\text{--}18$ per Å in the rest-frame interval $4000\text{--}4150 \text{ Å}$, that turned out to be sufficient to perform the stellar population analysis, as detailed below. In Tab. 1 we report the main properties of the seven spheroidal galaxies while their spectra are shown in Fig. 1. In each panel, the black curve plots the 8-hours MODS spectrum binned to 3.4 Å/pix and

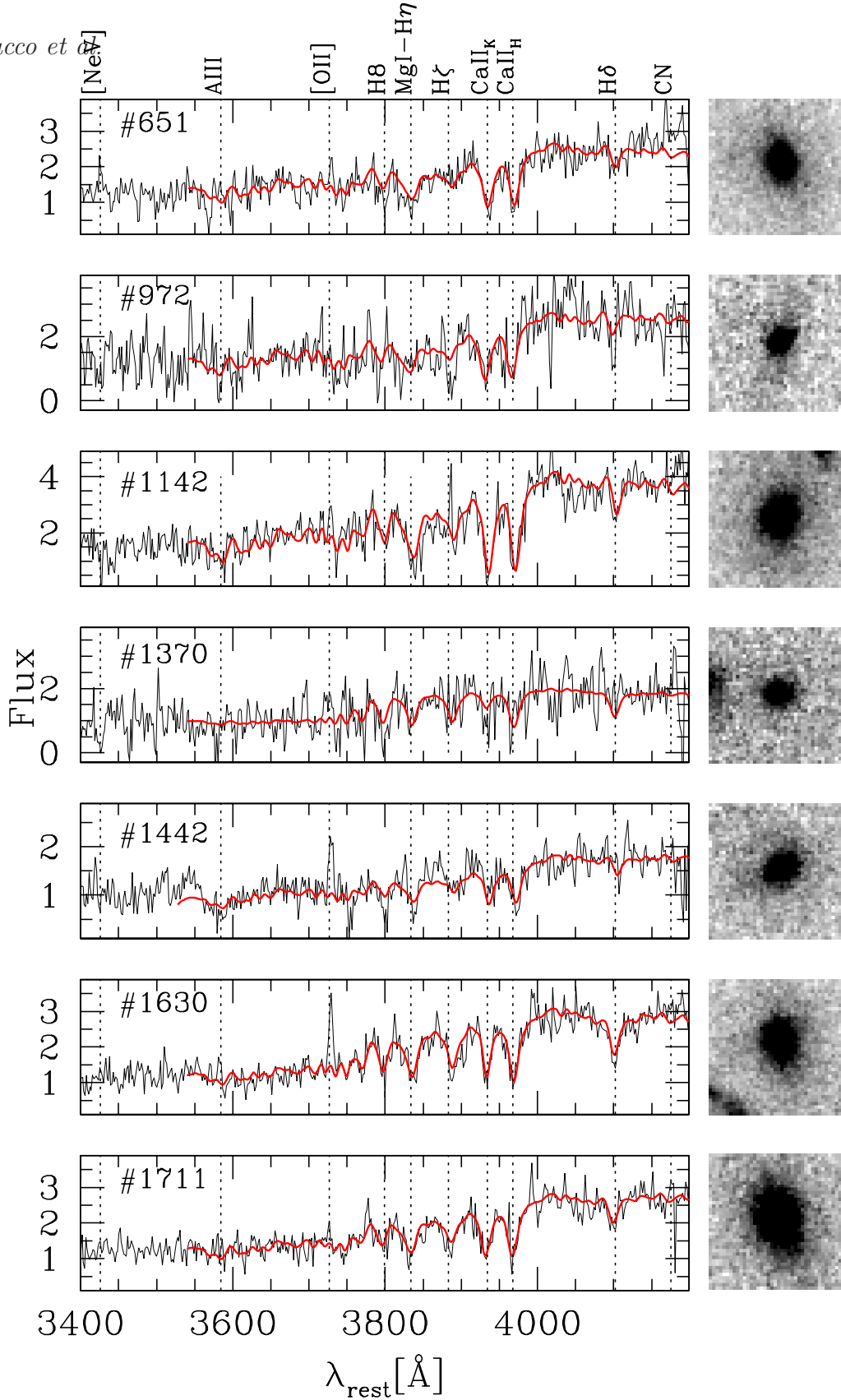


Figure 1. MODS spectra of the seven cluster members spheroidal galaxies for which we derived the velocity dispersion. The black curve is the observed spectrum arbitrarily normalized, binned to 3.4 \AA /pixel. These spectra have $S/N=[5-18]$ per Angstrom in the restframe of the galaxy, in the range $4000 < \lambda_{\text{rest}} < 4150 \text{\AA}$. The red curve is the best-fitting MILES model resulting from the pPXF spectral fitting. The dotted vertical lines mark the main spectral features labelled on top of the figure. To the right of each spectrum, the ACS-F850LP image (2×2 arcsec) of the target galaxy is shown.

the red curve is the best-fitting pPXF template. For each galaxy we also show the 2×2 arcsec ACS-F850LP image.

3.2 Emission lines: AGN and star formation

Two galaxies, namely #1442 and #1630 (see Tab. 1), show clearly [OII] line emission, while galaxy #651 shows a weak [OII] emission accompanied by the presence of [NeV] line emission. The high-ionization [NeV] λ 3426 emission line is considered a signature of nuclear activity (Schmidt et al. 1998; Gilli et al. 2010) since stars do not reach such high ionization potential (e.g. Haehnelt et al. 2001), therefore galaxy #651 most probably hosts an AGN. Apart from #651, there is no evidence for the presence of AGN in any other galaxy.

Assuming that [OII] emission is due to star formation (also for #651), we derived the star formation rate (SFR) from the relation

$$SFR = 1.4 \cdot 10^{-41} L([OII]) \quad (1)$$

where the SFR is expressed in $M_{\odot} \text{ yr}^{-1}$ and the luminosity $L([OII])$ in erg s^{-1} (Kennicutt 1998). The luminosity $L([OII])$ has been derived from the line flux $F([OII])$ measured on the calibrated spectra, $L([OII]) = 4\pi d_L^2 \cdot F([OII])$, where $d_L = 8449.9$ Mpc is the luminosity distance of the cluster at $z = 1.22$ for the adopted cosmology. The measured [OII] fluxes and the resulting SFR are reported in Tab. 1 for those galaxies for which we detect an [OII] line flux $> 1\sigma$. Our spectra show that at least two spheroids out of the seven show evidence of weak star formation, at a rate $< 4 M_{\odot} \text{ yr}^{-1}$, and one hosts an AGN.

We notice that, early-type galaxies with similar values of SFR (few $M_{\odot} \text{ yr}^{-1}$ or lower), are not rare and are observed both in the field and in cluster. SFRs of about $2-3 M_{\odot} \text{ yr}^{-1}$ are observed, for instance, in some early-types in cluster RDCSJ0848 at $z \sim 1.27$ (e.g. Jørgensen et al. 2014) as well as in the field at similar redshift (e.g. Cimatti et al. 2008; Belli et al. 2017). Also at lower redshift, some spheroidal galaxies exhibit low levels of star formation, both in clusters (e.g. Jørgensen et al. 2017) and in the field (e.g. Fukugita et al. 2004; Huang & Gu 2009; Yates & Kauffmann 2014; George 2017). This star formation activity in field early-types is thought to be fueled by inflowing gas and/or gas-rich minor mergers (Belli et al. 2017; George 2017). As to our seven spheroids, it is unlikely that star formation is fueled by inflowing gas, since gas and galaxies should be in thermal equilibrium in a cluster. Moreover, minor mergers are disfavoured in the cluster center regions given the large relative velocities of galaxies (e.g. Harrison et al. 2011; Treu et al. 2003). Thus, the low levels of star formation we observe could be the sign of a more complex or longer star formation history or the quenching phase of the main burst recently occurred. We further discuss the presence of star formation below.

3.3 Absorption line indices

We measured absorption line Lick indices, following the definition by Worthey & Ottaviani (1997) and Trager et al. (1998), and the indices by Rose (1994) in the rest-frame wavelength range covered by the observations. To perform

the measurements we made use of the software LECTOR¹. Besides these absorption indices, we measured the strength of the 4000Å break according to the D4000 definition by Bruzual (1983) (see also Gorgas et al. 1999) and the D_n index by Balogh et al. (1999). The uncertainties on the spectral indices have been derived through simulations according to the following procedure. For each observed 1D spectrum, we constructed a set of 100 simulated spectra having the same S/N of the real one. The S/N was evaluated in the rest-frame wavelength range 4000-4150 Å. The simulated spectra were obtained by summing to the best-fitting model template the 1D sky residual extracted from the final 2D spectra. In each simulated spectrum, the values of the residuals within the rest-frame wavelength range 3700-4400 Å were randomly shuffled. Then, for each simulated spectrum, we measured the indices using the same procedure used for the real spectra. We adopted as uncertainty on the measured index the median absolute deviation (MAD) resulting from the distribution of the 100 measurements.

The measured indices were corrected for galaxy velocity dispersion. The corrections were obtained for each galaxy by comparing the indices measured on the best-fitting model (smoothed to the σ of the galaxy), and those of the same model at the nominal resolution of the MILES spectral library. The corrected measured Lick indices and Rose's indices with their errors are summarized in Tab. 2 and Tab. 3 respectively.

4 STELLAR POPULATION PARAMETERS

The effective rest-frame wavelength range covered by our spectroscopic observations ($3500 < \lambda_{rest} < 4400 \text{ Å}$), does not provide us with enough spectral features suited to constrain the abundance ratios of α -elements (Ca, Mg, Si, Ti etc.). In particular, prominent tracers of Magnesium abundance, such as the Mgb spectral feature at $\lambda \sim 5270$, usually considered the best tracer of α -elements, fall outside our spectral range. For this reason, in the whole analysis, we limit ourselves to constrain the total metallicity $[Z/H]$ without considering the effect of $[\alpha/Fe]$.

4.1 Constraints from absorption line indices

In Fig. 2 the main Lick absorption indices (upper panel) and the main Rose's indices (lower panel) are plotted versus each other. The upper panels show the strength of CN3883 versus CaHK and D4000, and the strength of CaHK versus $H\delta_F$. The three plots are arranged to show two different metal lines, one against the other (CN3883 vs CaHK), and against two different age sensitive indices (D4000 and $H\delta_F$). The index CN3883 has been derived according to the definition of Davidge & Clark (1994) (see also Pickles 1985). The lower panels follow the same criterion of the upper ones showing the strength of $p[Fe/H]$ versus CaII(H/K) and $H\delta/Fe4045$, and the strength of CaII(H/K) versus D4000. The index $p[Fe/H]$ is metal-abundance sensitive, $H\delta/Fe4045$ increases with the stellar spectral type and the index CaII(H/K) is a

¹ http://www.iac.es/galeria/vazdekis/vazdekis_software.html

Table 2. Lick spectral indices.

| ID | CN3883 (mag) | CaHK (Å) | D4000 | D _n | Hδ _A (Å) | Hδ _F (Å) | CN1 (mag) | CN2 (mag) | Ca4227 (Å) | G4300 (Å) |
|------|-----------------|-------------|-----------|----------------|------------------------|------------------------|--------------|--------------|---------------|--------------|
| 651 | 0.27±0.05 | 23.6±2.3 | 1.86±0.05 | 1.51 | 3.1±2.0 | 3.7±1.0 | -0.21±0.05 | -0.20±0.06 | 4.2 ±0.8 | 4.9±1.4 |
| 972 | 0.32±0.05 | 22.4±2.6 | 2.13±0.05 | 2.00 | 1.3±2.2 | 4.6±1.2 | 0.17±0.05 | 0.25±0.07 | 3.9 ±0.9 | 1.2±1.6 |
| 1142 | 0.20±0.04 | 30.6±2.0 | 2.19±0.04 | 1.75 | 0.7±1.7 | 4.1±0.9 | 0.03±0.04 | 0.07±0.05 | 0.2 ±0.7 | 10.4±1.2 |
| 1370 | 0.04±0.06 | 19.8±3.0 | 1.52±0.06 | 1.30 | -2.8±2.5 | 0.2±1.3 | 0.09±0.06 | 0.13±0.08 | 3.3 ±1.0 | 6.2±1.8 |
| 1442 | 0.15±0.05 | 17.7±2.3 | 1.77±0.05 | 1.33 | -2.3±2.0 | 2.0±1.0 | -0.17±0.05 | 0.17±0.06 | -0.9 ±0.8 | 12.6±1.4 |
| 1630 | -0.01±0.04 | 10.0±2.0 | 1.82±0.04 | 1.48 | 7.9±1.7 | 5.9±0.9 | -0.19±0.04 | -0.15±0.05 | -1.6 ±0.7 | 2.7±1.2 |
| 1711 | 0.15±0.03 | 18.5±1.8 | 1.84±0.03 | 1.54 | 3.1±1.5 | 3.1±0.8 | 0.01±0.03 | 0.01±0.04 | 3.3 ±0.6 | 6.8±1.0 |

The indices are corrected for galaxy velocity dispersion (see Sec. 3.3).

Table 3. Same as Tab. 2 but for Rose indices.

| ID | 3888/3859 | CaII(H/K) | Hδ/FeI[4045] | Hδ/FeI[4063] | p[Fe/H] |
|------|-----------|-----------|--------------|--------------|---------|
| 651 | 1.1±0.4 | 0.8±0.4 | 1.1±0.2 | 1.1±0.2 | 1.0±0.2 |
| 972 | 0.3±0.4 | 0.9±0.4 | 0.3±0.2 | 0.4±0.2 | 1.4±0.2 |
| 1142 | 0.8±0.3 | 1.2±0.3 | 0.9±0.2 | 0.9±0.2 | 1.3±0.1 |
| 1370 | 0.7±0.5 | 0.9±0.5 | 0.8±0.4 | 0.8±0.4 | 1.3±0.3 |
| 1442 | 0.8±0.4 | 0.7±0.4 | 1.1±0.2 | 1.1±0.2 | 1.0±0.2 |
| 1630 | 0.5±0.3 | 1.0±0.3 | 0.6±0.2 | 0.6±0.2 | 1.0±0.1 |
| 1711 | 0.7±0.2 | 0.9±0.2 | 0.7±0.1 | 0.7±0.1 | 1.1±0.1 |

good tracer of the presence of very young populations, being sensitive to A-type stars (Rose 1994; Longhetti et al. 1999).

The seven spheroidal galaxies here analyzed are shown with different (filled) symbols according to the legend in the inset. Galaxies in cluster RDCS0848 (LinxW) at $z = 1.27$, whose measurements have been obtained by Jørgensen et al. (2014) (green filled squares) are also shown. For this cluster, we considered the galaxies belonging to samples #5 and #4 of Tab. 7 in Jørgensen et al. (2014) for which measurements are available. For comparison with lower redshift data, we show the measured indices for galaxies in cluster MS0451.6 at $z \simeq 0.54$ (open cyan triangles) and in cluster RXJ1226.9 at $z \simeq 0.89$ (open magenta squares) by Jørgensen & Chiboucas (2013).

Solid curves are model predictions based on MILES SSPs (Vazdekis et al. 2010) with Chabrier initial mass function (IMF) (Chabrier 2003). The models shown are plotted in the age range [0.1,5] Gyr and refer to three different values of metallicity [Z/H]: -0.71 (dark green curve), 0.0 (orange line) and +0.22 (dark red curve). We also considered the two cases of a very young (0.06 Gyr) population representing 0.1% of the stellar mass with [Z/H]=-0.71 (cyan curve) and [Z/H]=0.22 (blue curve) superimposed to an underlying dominant [Z/H]=0 population. Dashed (fuchsia) curve represents the prediction based on BC03 SSPs (Bruzual & Charlot 2003) with solar metallicity and Chabrier IMF, in the same age range. No significant differences arise among the different models considered. Therefore, the results of the following analysis are independent of the adopted models.

In spite of the degeneracy between age and metallicity affecting most of the indices, the diagnostic diagrams in Fig. 2, can be used to constrain relative differences in age and metallicity among galaxies in our sample. The deviation from SSPs could suggest a more complex history of

star formation than the one described by a SSP as found, for instance, by Lonoce et al. (2014) for field early-type galaxies at ~ 1 . Whether this is the case, it will be explored in the next section through full spectral fitting.

Galaxies #1370, #1442 and #1630 lie on or below the lowest metallicity track in the CaHK vs Hδ_F diagram, the one less affected by the degeneracy, while galaxies #651, #972 and #1142 lie above the highest metallicity track and galaxy #1711 lies in between. This behaviour is due to the fact that the strength of CN3883 in galaxies #1370, #1442, #1630 and #1711 is significantly weaker than in galaxies #651, #972 and #1142, as visible also from the CN3883 vs CaHK diagram. Also the p[Fe/H] index tends to be weaker for galaxies #1442, #1630 and #1711 with respect to the other galaxies in the sample. These differences are consistent with galaxies #1370, #1442, #1630 and #1711 having lower metallicity than the remaining three galaxies.

As to the age, we notice that the D4000 is stronger in galaxies #651, #972 and #1142 than in the other galaxies, in agreement with the CaHK index being stronger in these three galaxies, and with the CaII(H/K) close to unity for #972 and #1142. The possible presence of weak star formation (see §3.2) superimposed to an older population, could justify the lower value of this index in galaxy #651. These three galaxies tend to occupy the end at oldest ages of the SSP tracks in the diagrams showing metal-sensitive index vs age-sensitive index (e.g. CN3883/CaHK and CN3883/D4000), at odds with the other galaxies. Thus, the picture is consistent with an age for #651, #972 and #1142 older than for the other galaxies.

Galaxies #1630 and #1442 are among the youngest galaxies in our sample. They both show star formation (see Tab. 1) but are characterized by different values of the indices, with the exception of the D4000, not significantly different. Galaxy #1630 occupies the lowest-age end of the SSP

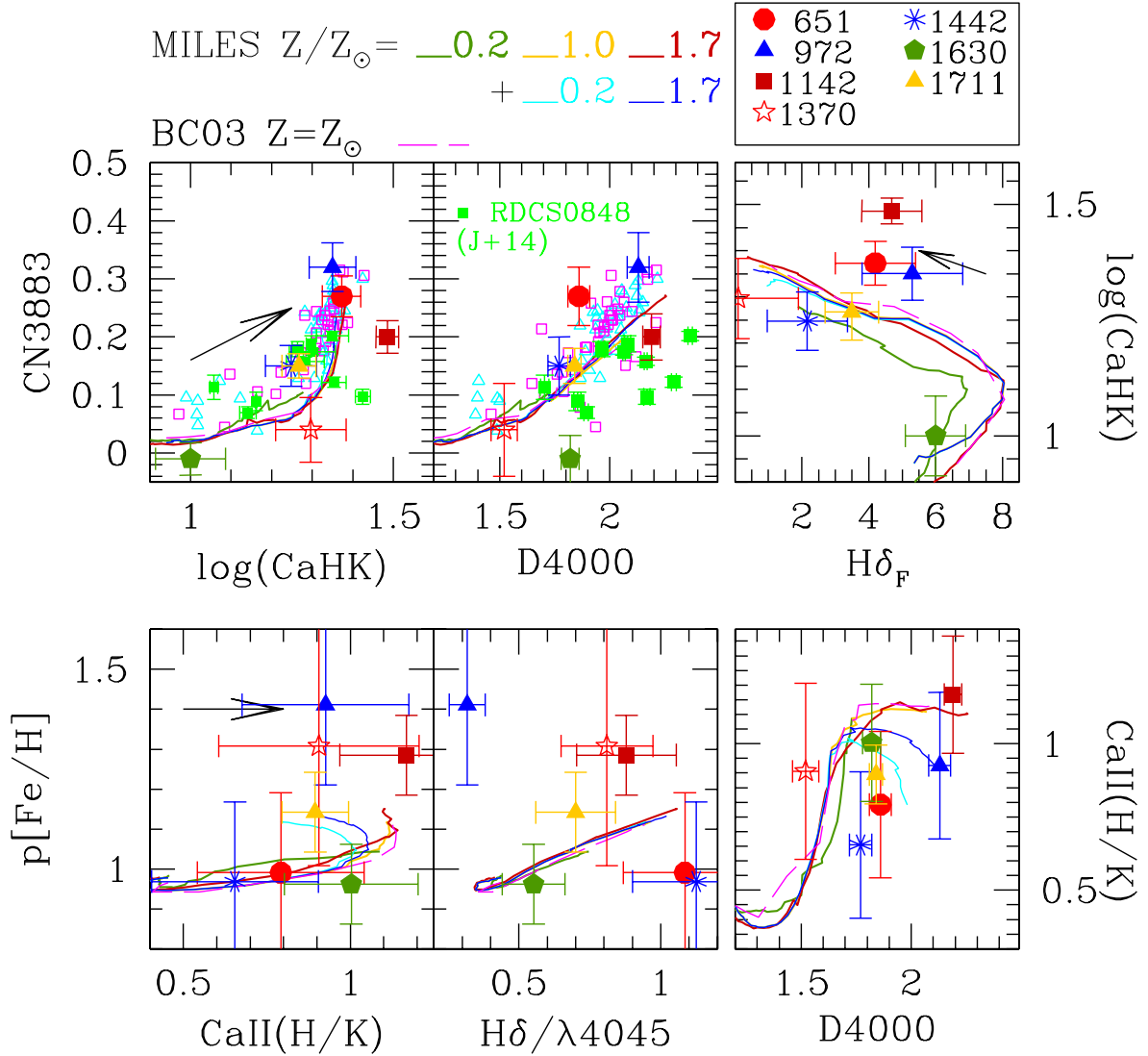


Figure 2. Absorption line strengths versus each other. Upper panels - Absorption Lick indices. The seven spheroidal galaxies belonging to the cluster XLSSJ0223 whose measurements are reported in Tab. 2, are represented by the different symbols reported in the inset. Green filled square are measurements of galaxies in the cluster RDCS0848 at $z \sim 1.27$ (Jørgensen et al. 2014). Open (cyan) triangles and (magenta) squares are galaxies in the clusters MS0451.6 at $z \simeq 0.54$ and RXJ1226.9 at $z \simeq 0.89$ respectively (Jørgensen & Chiboucas 2013). Solid curves are predictions from MILES SSP models (Vazdekis et al. 2010) for the three different metallicity values reported in the figure legend and plotted in the age interval 0.1-5 Gyr. The cyan and blue thin curves are the Z_{\odot} SSP in the interval 0.1-5 Gyr with the addition of a young (0.06 Gyr) component (0.5% of the mass) with $Z=0.2Z_{\odot}$ and $Z=1.7Z_{\odot}$, respectively. The dashed (fuchsia) curve show predictions from BC03 SSP model (Bruzual & Charlot 2003) with Chabrier IMF and solar metallicity in the same age interval. The arrows indicates the direction in which the age increases following the models. Observed indices are corrected for velocity dispersion. Lower panels - Rose's (Rose 1994; Rose et al. 1994) absorption line indices. The values are reported in Tab. 3. Symbols are as in the upper panels.

tracks in most diagrams. It is characterized by the highest $H\delta$ indices and by the lowest CaHK. The Rose's index CaII(H/K), whose CaII(H) line is sensitive to young stars, is close to one suggesting that the whole stellar population of this galaxy is genuinely young. For comparison, galaxy #1442 has a higher CaHK and lower $H\delta$ indices, accompanied by a CaII(H/K) lower than unity. This would suggest that the newly formed stars are superimposed to an older population.

4.2 Absorption lines fitting

As a first step to characterize stellar population properties of the seven spheroidal galaxies in XLSSJ0223, we have derived their age and metallicity, $[Z/H]$, by comparing observed line-strengths to predictions from SSP models with varying age and metallicity. To this effect, we use the same set of MILES SSP models (Vazdekis et al. 2010) as for spectral fitting (see Sec. 5.1), namely SSPs based on PADOVA isochrones (Girardi et al. 2000), with a Chabrier IMF, ages in the range

Table 4. Age and metallicity estimates resulting from absorption lines fitting

| ID | Age (Gyr) | [Z/H] |
|------|---------------------|-------------------------|
| 651 | $2.2^{+0.8}_{-0.4}$ | $-0.31^{+0.44}_{-0.17}$ |
| 972 | $1.9^{+1.3}_{-0.7}$ | $+0.02^{+0.19}_{-0.51}$ |
| 1142 | $2.8^{+1.6}_{-0.6}$ | $+0.16^{+0.06}_{-0.31}$ |
| 1370 | $1.3^{+1.0}_{-0.3}$ | $-0.05^{+0.18}_{-0.57}$ |
| 1442 | $1.9^{+1.5}_{-0.8}$ | $-0.52^{+0.50}_{-0.77}$ |
| 1630 | $0.9^{+0.2}_{-0.1}$ | $+0.01^{+0.20}_{-0.39}$ |
| 1711 | $1.5^{+0.7}_{-0.4}$ | $-0.10^{+0.32}_{-0.52}$ |

from 0.06 to 4.5 Gyr, and metallicity in the range -2.32 – $0.22 Z_{\odot}$.

The fitting is performed by minimizing the expression:

$$\chi^2(\text{age}, [Z/H]) = \sum_j \frac{(O_j - M_j)^2}{s_j^2} \quad (2)$$

where the index j runs over the selected set of Lick spectral indices in the rest-frame range 3500–4400 Å (see Tab. 2), O_j and M_j are observed and model index values (the latter depending on age and $[Z/H]$), and s_j are uncertainties on observed indices. The resulting best-fitting age and metallicity are reported in Tab. 4. The quoted errors are obtained by running the fitting procedure on a set of simulated spectra, having the same S/N as the observed spectra.

It is worth noting that, as expected, the age and metallicity values in Tab. 4 confirm the general trends obtained from the diagnostic diagrams in Fig. 2 (see Sec. 4.1), namely that galaxy #1630 is the youngest object in our sample, galaxies #651, #972, and #1142 are the oldest, while galaxies #1370 and #1442 tend to have lower metallicities than the remaining systems.

5 CONSTRAINTS ON STAR FORMATION HISTORY

5.1 Full spectral fitting

To recover the main properties of the stellar populations of the seven galaxies, the mean stellar age and metallicity, and to constrain their star formation history (SFH), we also used full spectral fitting. In this approach, one assumes that the observed spectrum is the superposition of few simple stellar populations (SSPs), with age Age_i and metallicity Z_i , each one contributing with a different weight, extracted from a larger base of models of different ages and metallicities. To perform the spectral synthesis and find the best-fitting linear combination of SSPs, we used the code **STARLIGHT** (Cid Fernandes et al. 2005, 2007; Mateus et al. 2007; Asari et al. 2007).

We adopted as reference base of models the SSPs from the MILES-based library (v 11.0) of Vazdekis et al. (2010), covering the wavelength range 3540–7400 Å at a spectral resolution of 2.5 Å. We considered Chabrier IMF and two different sets of *Base* SSPs: the first one based on the PADOVA00 isochrones (Girardi et al. 2000) and the second one on the BaSTI isochrones (Pietrinferni et al. 2004). For both these

sets of models, the ages considered are ~ 30 in the range [0.06; 4.5] Gyr while the metallicities are 7 for the PADOVA set in the range $[-2.23; 0.22]$, and 9 for the BaSTI set in the range $[-2.27; 0.26]$. We allowed for internal reddening in the **STARLIGHT** fits, by considering both the Cardelli (CCM; Cardelli et al. 1989) and the Calzetti (HZ5; Calzetti et al. 2000) extinction laws in the fit. The fitting was performed in the wavelength range 3600–4400 Å.

To assess the robustness of the derived stellar population properties with respect to the models adopted in the fitting, we also considered a base composed of BC03 SSPs (Bruzual & Charlot 2003) with Chabrier IMF, 20 ages in the range [0.06; 4.5] Gyr and 5 metallicities in the range $[-1.7; 0.4]$, and a base composed of Maraston & Strömbäck (2011) MILES-based models (MS11 hereafter) with Chabrier IMF and including 20 ages in the range [0.06; 4.5] Gyr and 5 metallicities in the range $[-2.3; 0.3]$. The results of the fitting with these two sets of models are summarized in Tables A1 and A2, respectively.

5.2 Ages and metallicities derivation

We defined the luminosity-weighted age $\langle \text{Age} \rangle_L$ and metallicity $[Z/H]_L$ as

$$\begin{aligned} \text{Age}_L &= \sum_i x_i \text{Age}_i \\ [Z/H]_L &= \log \sum_i x_i Z_i / Z_{\odot} \end{aligned} \quad (3)$$

where x_i is the fractional contribution of the i -th SSP considered in the synthesis, while Age_i and Z_i are its age and metallicity. Analogously, we defined the stellar mass-weighted age and metallicity as

$$\begin{aligned} \text{Age}_M &= \sum_i m_i \text{Age}_i \\ [Z/H]_M &= \log \sum_i m_i Z_i / Z_{\odot} \end{aligned} \quad (4)$$

where m_i is the fraction of stellar mass of the i -th SSP.

In Tab. 5 the luminosity-weighted and the mass-weighted age and metallicity values resulting from the spectral fitting are reported for each galaxy, together with the reduced χ^2 of the best-fitting model. The values refer to results obtained with the set of SSPs based on PADOVA isochrones. The corresponding best-fitting synthetic spectra are shown in Figure 3. Results based on BaSTI isochrones are similar to those obtained with PADOVA models, and are not shown here for brevity reasons, with differences in age and metallicity smaller than 20%, and 0.15dex, respectively. The two extinction laws produce negligible differences. The values of metallicity and age obtained through the spectral fitting confirm those previously derived in §4: galaxies #651, #972, and #1142 are the oldest in our sample while galaxy #1620 is the youngest; galaxies #1370 and #1442 tend to have lower metallicities than the others.

The errors on age and metallicity are the confidence intervals at 68% confidence level of the solutions in the Age- $[Z/H]$ space. They have been obtained considering all the fitting solutions within 1σ from the best-fitting one. To this end, we compared the reduced- χ^2 of all the solutions with the reduced- χ^2 of the best-fitting one making use of the

Table 5. Age and metallicity estimates resulting from spectral fitting

| ID | Age _L (Gyr) | [Z/H] _L | Age _{M*} (Gyr) | [Z/H] _{M*} | A _V (mag) | z _f | n(SSPs) | χ _ν ² |
|------|-------------------------------------|---|-------------------------------------|---|-------------------------|----------------|---------|-----------------------------|
| 651 | 2.7 ^{+1.0} _{-0.7} | +0.09 ^{+0.13} _{-0.42} | 3.0 ^{+0.8} _{-0.7} | +0.09 ^{+0.13} _{-0.42} | 0.0 | 3.4 | 4 | 0.89 |
| 972 | 3.4 ^{+0.9} _{-0.6} | +0.16 ^{+0.06} _{-0.16} | 4.4 ^{+0.1} _{-0.5} | +0.21 ^{+0.01} _{-0.21} | 0.3 | >6.5 | 2 | 0.82 |
| 1142 | 2.3 ^{+1.2} _{-0.2} | +0.21 ^{+0.01} _{-0.21} | 2.4 ^{+1.4} _{-0.2} | +0.22 ^{+0.00} _{-0.22} | 0.8 | 2.6 | 2 | 0.93 |
| 1370 | 1.3 ^{+1.8} _{-0.2} | -0.27 ^{+0.49} _{-0.12} | 1.9 ^{+0.8} _{-0.5} | -0.10 ^{+0.32} _{-0.61} | 1.0 | 2.0 | 2 | 0.80 |
| 1442 | 1.7 ^{+0.7} _{-0.5} | -0.18 ^{+0.44} _{-0.21} | 2.7 ^{+0.2} _{-0.5} | -0.01 ^{+0.23} _{-0.38} | 0.9 | 2.9 | 4 | 0.90 |
| 1630 | 1.2 ^{+0.6} _{-0.3} | -0.13 ^{+0.39} _{-0.26} | 1.4 ^{+0.7} _{-0.2} | -0.22 ^{+0.44} _{-0.17} | 1.2 | 1.9 | 3 | 0.88 |
| 1711 | 1.7 ^{+0.2} _{-0.5} | +0.05 ^{+0.17} _{-0.05} | 2.1 ^{+0.2} _{-0.5} | +0.18 ^{+0.04} _{-0.18} | 0.7 | 2.4 | 4 | 0.90 |

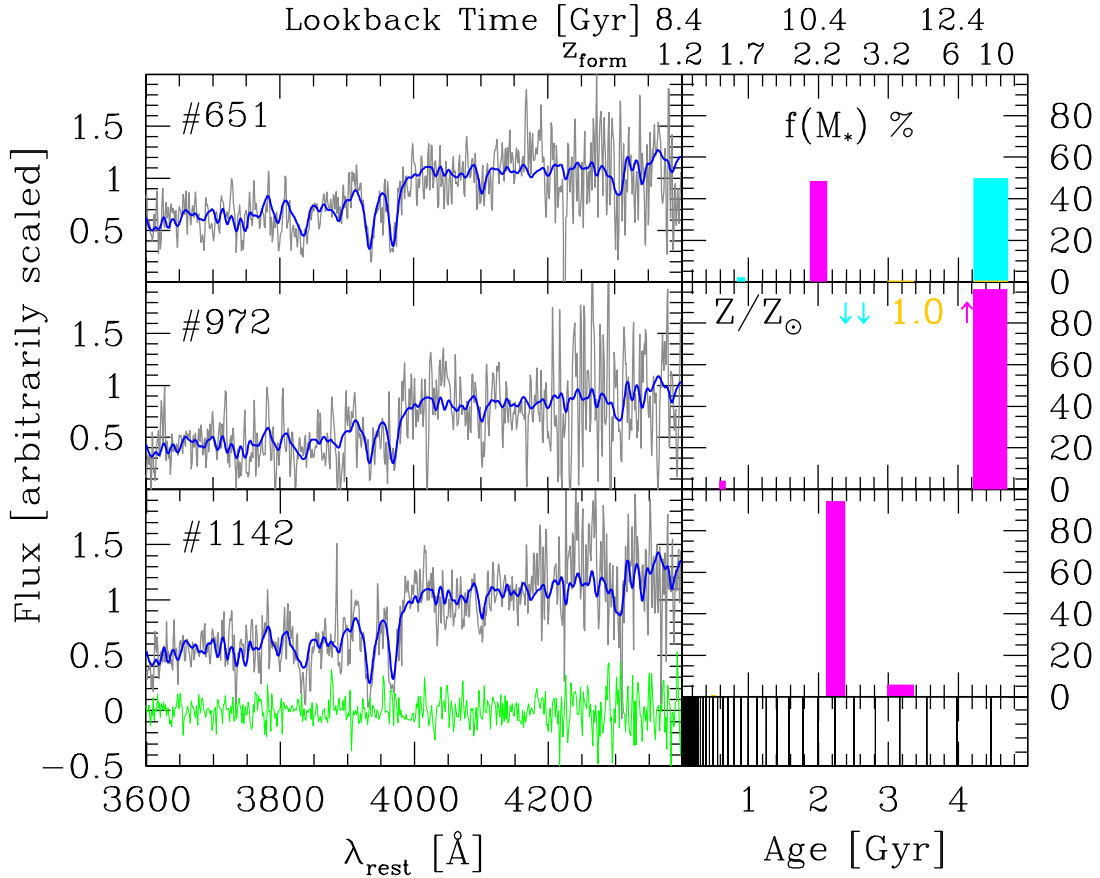


Figure 3. Results of the spectral synthesis for galaxies #651, #972 and #1142. Left panels - The best-fitting composite spectrum (blue curve) resulting from the spectral synthesis performed with STARLIGHT is superimposed to the observed spectrum (dark gray curve) binned to 3.4Å/pix. The green curve in the bottom panel represents the typical sky residuals extracted from the image of galaxy #1142. Right panels - Star formation history of galaxies. Fraction of stellar mass of each SSP contributing to the best-fitting spectrum as a function of lookback time and formation redshift (top x-axis). Different colours encode different values of metallicity: cyan $Z < Z_{\odot}$ (cyan down arrows in the legend), yellow $Z = Z_{\odot}$, magenta $Z > Z_{\odot}$ (magenta upward arrows in the legend). The bar code on the bottom represents the grid of ages considered in the base of SSPs adopted to run STARLIGHT (see the text).

F-test. Due to the fact that errors on age and metallicity are anti-correlated, (see, e.g., Thomas et al. 2005), the confidence intervals should be read jointly in the sense that, older (higher) values of age (metallicity) correspond to lower (younger) values of metallicity (age) with respect to the best-fitting values. It is worth noting that predictions of MILES-SSPs for a certain range of very young ages and very low metallicities, (age < 0.1 Gyr and $[Z/H] < -1.5$) are flagged as

unsafe² by Vazdekis et al. (2010). We note, however, that there are no SSPs within the unsafe range contributing to the fitting solutions.

As can be seen from Tab. 5, luminosity-weighted and mass-weighted metallicities do not differ significantly (con-

² <http://www.iac.es/proyecto/miles/pages/ssp-models/safe-ranges.php>

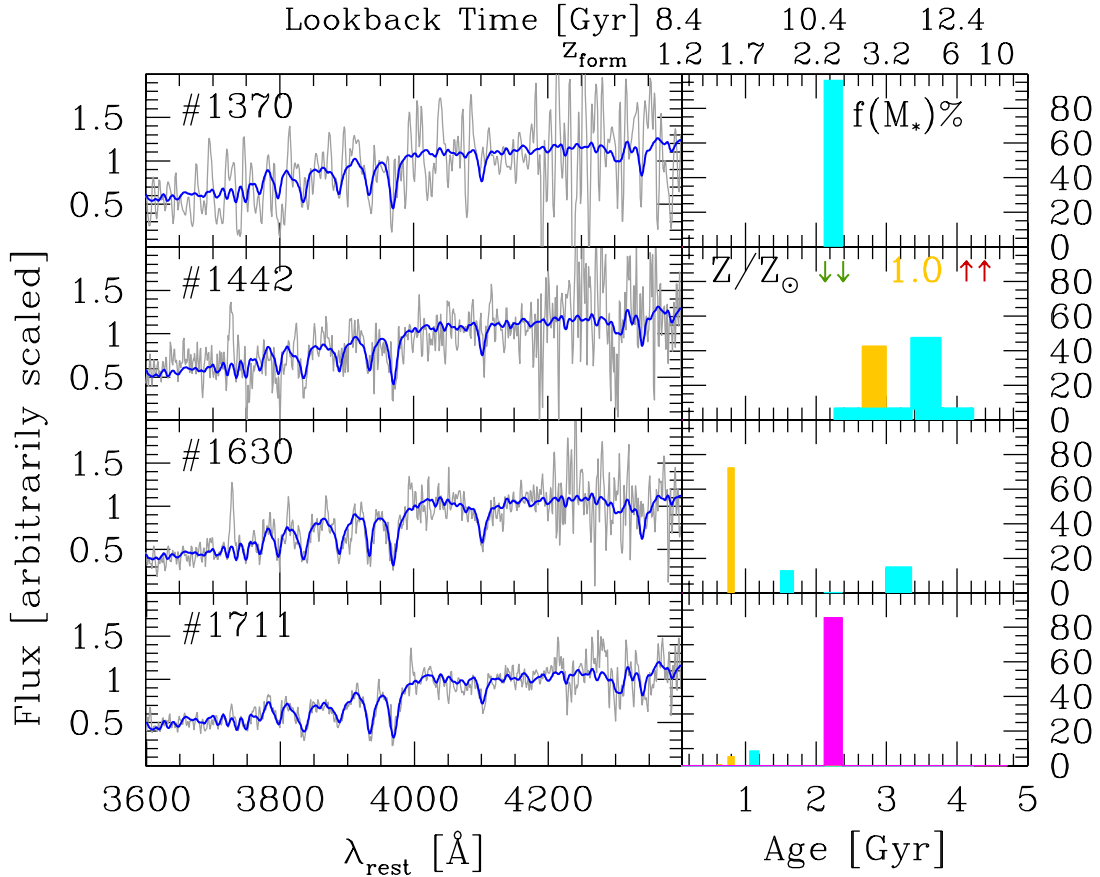


Figure 3 (Cont.). Results of the spectral synthesis for galaxies #1370, #1442 and #1630 and #1711.

sidering the errors), since the M/L ratio plays a secondary role in the derivation of this quantity. The best fitting metallicity values never reach the extremes of the range considered, with the exception of the galaxy #1142, close to the maximum metallicity value allowed in the reference grid of SSPs. Finally, we emphasize that despite to the well-known age-metallicity degeneracy (whereby the effect of an older age is almost exactly compensated by that of a lower metallicity in the spectral synthesis), our best-fitting age and metallicity are not anti-correlated, showing again the robustness of the results.

The resulting metallicity estimates for the 7 spheroids lie within 0.2 dex from the solar value with a median value $\langle [Z/H]_M \rangle = 0.09 \pm 0.16$. This is in agreement with the results obtained in §4 based on absorption line indices (see Tab. 4). The above results and considerations also hold for the estimates of stellar age, whose median value is $\langle \text{Age}_M \rangle = 2.4 \pm 0.6$ Gyr.

5.3 Metallicity variation and evolution with redshift

In the upper panel of Fig. 4, the metallicities of the 7 cluster spheroids at $z = 1.22$, as reported in Tab. 5, are compared with the metallicities of galaxies in clusters at lower redshift and with the metallicities of field galaxies of comparable mass at lower and higher redshifts. The figure shows

representative median metallicity values of galaxies in clusters in the redshift range $0.2 < z < 0.9$ from Jørgensen et al. (2017) and Jørgensen & Chiboucas (2013), the median value of field early-type galaxies at $z \sim 0.7$ from Gallazzi et al. (2014) and from the eBOSS sample (Comparat et al. 2017), median values of early-type galaxies at different redshift bin from Ferreras et al. (2018), the mean value of field galaxies at $z \sim 1.6$ from Onodera et al. (2015) and the single measurements of metallicity obtained by Lonoce et al. (2015) at $z \sim 1.4$, Kriek et al. (2016) at $z \sim 2.1$ and Morishita et al. (2018) at $z \sim 2.2$.

The stellar metallicity of cluster early-type galaxies remains nearly constant above the solar value ($[Z/H]=0$) up to $z \sim 1.3$. We notice that the median value ($[Z/H]_m = 0.09$) of the 7 spheroids at $z \sim 1.22$ is slightly lower than the median value $[Z/H]=0.24$ estimated by Jørgensen et al. (2017) in the range $0.2 < z < 0.9$. However, this difference cannot be considered as an hint for a decrease of $[Z/H]$ with redshift, as there is also one cluster (MS0451 at $z \sim 0.54$) in the Jørgensen et al. (2017) sample, whose median value of $[Z/H]$ (~ 0.1) is fully consistent with that we measure for galaxies in XLSSJ0223. Thus, it might be just related to a cluster-to-cluster variation in $[Z/H]$.

Overall, the nearly stable and constant metallicity value obtained from independent analysis over the redshift range $0 < z < 1.3$ shows that no significant metallicity evolution for the population of cluster early-types has taken place over the

last 9 billion years. Thus, for the cluster spheroidal galaxies at $z \sim 1.3$, no significant additional star formation and chemical enrichment are required to join the present-day population of cluster early-type galaxies.

Fig. 4 shows also that stellar metallicity values above solar seem to be common in high-mass galaxies, at least up to $z \sim 2$. The figure suggests that there are no significant differences between the metallicity of cluster and field early-types at the redshift probed. We notice, however, that studies of local samples do not reach concordant results about this issue. Some of them find no significant differences as a function of the environment but, rather, of the mass of galaxies, with environment playing a role in less massive galaxies (e.g. Bernardi 2009; Thomas et al. 2010; McDermid et al. 2015). On the contrary, other studies point toward significant differences, with galaxies in lower density environments being less metal rich (e.g. Cooper et al. 2008; La Barbera et al. 2010c).

5.4 Stellar age and star formation history

The median stellar age of the seven spheroids, $\langle \text{Age}_M \rangle = 2.4 \pm 0.6$ Gyr, implies a median formation redshift $\langle z_f \rangle \sim 2.6^{+0.7}_{-0.5}$. This value is slightly higher (not significantly, given the uncertainties) than the median formation redshift ($z_f \sim 2$) derived from the stellar ages and from the fundamental plane for early-type galaxies in clusters at $z < 0.9$ by Jørgensen et al. (2017) and Jørgensen & Chiboucas (2013). It is consistent with the median formation redshift $z_f \sim 2.2$ derived by Woodrum et al. (2017) for field early-type galaxies at $z \sim 1$ with velocity dispersion larger than 170 km/s (as it is the case for six out of our seven spheroids; see Fig. 5).

The lower panel of Fig. 4 shows the stellar age of galaxies as a function of redshift for the same data samples considered in the upper panel. The different curves show the prediction of stellar age for different values of the formation redshift in the case of passive ageing. The median stellar age of early-type galaxies in clusters at $z < 0.9$ varies from cluster to cluster and, for some of them, it is consistent with formation redshifts even higher than our result ($z_f > 3$).

Contrary to metallicity, there is a significant scatter in the ages of the seven spheroids, the largest difference being $\Delta \text{Age} \sim 3$ Gyr, independently of considering mass-weighted or light-weighted values. To estimate the significance of the scatter, we constructed $N=1000$ random realizations of the age distribution of our sample, assuming a constant mean age for all galaxies. For each galaxy, we assumed a normal distribution with lower (upper) σ given by the lower (upper) relative error on its age, and the same central value of 2.4 Gyr, the median age of our sample. For each realization, we estimated the standard deviation of the age distribution σ_{age} . From the distribution of σ_{age} among different realizations, we obtained an expected scatter of measurement $\sigma_m = 0.57^{+0.33}_{-0.23}$ Gyr for our sample. Subtracting in quadrature the σ_m to the observed standard deviation of age estimates for our sample (~ 1 Gyr) we obtained an intrinsic age scatter of $\sigma_I = 0.78^{+0.24}_{-0.17}$ Gyr, which is significantly larger than zero at ~ 4 sigma level.

The scatter in stellar age corresponds to a significant spread of the formation redshift (see Tab. 5 and Fig. 4). The seven spheroids at $z \sim 1.3$ are on the ageing tracks

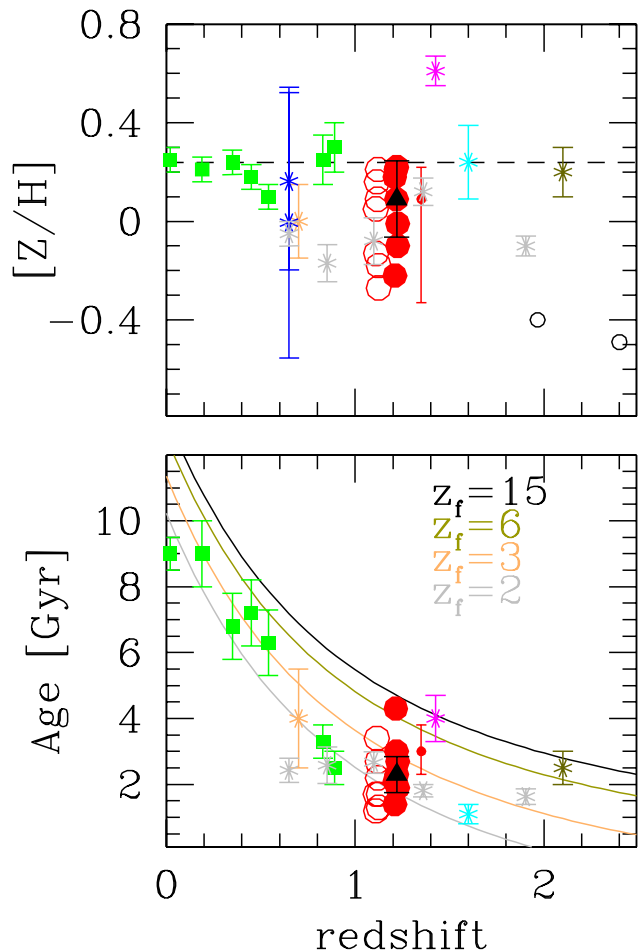


Figure 4. Stellar metallicity (upper panel) and Age (lower panel) of galaxies versus redshift. The red filled circles are the mass-weighted values obtained for the 7 spheroidal galaxies in the cluster XLSS0223 at $z = 1.22$ reported in Tab. 5, the black triangle is the median value. The luminosity-weighted values are the open red circles offset by -0.1 in redshift for clarity. The small red dot with errorbar at $z = 1.35$ shows, as example, the confidence intervals for the galaxy #651. The green filled squares are the median values of cluster early-type galaxies at $0 < z < 0.9$ from Jørgensen & Chiboucas (2013) and Jørgensen et al. (2017). Skeletal symbols represent metallicity and age values of field early-type galaxies at different redshifts from the literature: the blue points at $z \sim 0.65$ are the median values of eBOSS galaxies with masses $\log(M_*)$ in the ranges $[10.7-10.9] M_\odot$ ($Z/H=0.005$) and $[10.9-11.1] M_\odot$ ($Z/H=0.16$) (Comparat et al. 2017), the orange point at $z = 0.7$ is the median value of galaxies in the mass range $10.85 < \log(M_*/M_\odot) < 11$ from Gallazzi et al. (2014), the light-gray points are median values of early-type galaxies from Ferreras et al. (2018), the fuchsia point at $z = 1.4$ is a massive ($\log M_* > 11 M_\odot$) galaxy from Lonoce et al. (2015), the cyan point at $z \sim 1.6$ has been derived from the stacked spectra of 24 galaxies (Onodera et al. 2015), the brown point is the measurement for a massive galaxy at $z = 2.1$ (brown, Kriek et al. 2016), the two open circles at $z \sim 2$ (upper panel only) are measurements of two lensed galaxies (Morishita et al. 2018). The dashed line in the upper panel is the median value $[Z/H]=0.24$ at $0 < z < 0.9$ (from Jørgensen et al. 2017). The curves in the lower panel are predictions for passive evolution for different values of formation redshift z_f , as labelled in the figure.

that would lead them to join the present-day population of cluster early-type galaxies. However, this does not mean that they all have to evolve passively to $z=0$. The large scatter of their ages, indeed, leaves room to possible minor episodes of star formation that some of them could experience during the following 9 billion years.

Table 5 reports also the number of SSPs, $n(\text{SSPs})$, contributing to the synthesis of the spectrum. The contribution of each component, in terms of stellar mass fraction, metallicity and age, that is the star formation history (SFH) of each galaxy, is shown in the right panels of Figure 3. The histograms represent the stellar mass fraction of each component, the colour identifies the metallicity (green sub-solar, yellow solar, red above solar), the bar-code on the bottom of Fig. 3 shows the ages of the SSPs considered. The lookback time and the formation redshift corresponding to the ages of the SSPs are also shown on the top x-axis of the figures.

Given the small number of galaxies, we are not in position to study the dependence of the SFH of early-type galaxies at $z \sim 1.3$ on galaxy mass as done, e.g., by Thomas et al. (2005, 2010), de La Rosa et al. (2011) or McDermid et al. (2015), since our results would be dominated by the intrinsic scatter among the galaxies. Hence, we consider here only the overall features of the sample.

In most cases, the bulk of the stellar mass is formed in a single main episode of star formation, as for galaxies #972, #1142, #1370, #1711, and also for galaxy #1630, the youngest galaxy most likely in quenching phase (see §4.1). Hence, these galaxies are characterized by a similar SFH. However, their mass-weighted ages, that represent the epoch of formation of most of their stellar content, differ significantly, pointing to different formation epochs. In the remaining cases, the SFH is protracted over longer time or distributed among different episodes of star formation, as in the case of #651, and still not ceased, as for #1442. The formation redshift of the bulk of galaxy stellar mass, is consistent with the mean value found by de La Rosa et al. (2011) and McDermid et al. (2015) (lookback time >10 Gyr) for galaxies with similar dynamical mass ($\log(M_{\text{dyn}}) > 11 M_{\odot}$), even if the SFH of some of our spheroids implies a larger lookback time.

Overall, our results show that the population of massive spheroids, in this cluster at least, is not coeval and their stellar populations have been formed at significant different epochs.

6 AGE AND METALLICITY SCALING RELATIONS

In Fig. 5, the age and the stellar metallicity of the seven cluster spheroidal galaxies are plotted versus their stellar velocity dispersion σ_e [km s^{-1}], dynamical mass $M_{\text{dyn}} = 5\sigma_e^2 R_e / G$ [M_{\odot}] and stellar mass density within the effective radius $\Sigma_e = 0.5M^*/\pi R_e^2$ [$M_{\odot} \text{ pc}^{-2}$]. Velocity dispersion measurements are from Saracco et al. (2018, in preparation). Given the small number of galaxies of our sample, it is beyond the scope of our analysis to establish the relationships between stellar populations properties and structural properties in early-type galaxies at $z \sim 1.3$. Our aim is to assess whether correlations can be detected in our data, hence whether they are already present at this redshift, and how

the properties of these spheroidal galaxies compare with the local relations.

In Fig. 5, the light-weighted parameters instead of the mass-weighted ones, are highlighted by red filled circles to make the comparison with local relations, based on light-weighted values, easier. The age and metallicity versus σ relations found by Jørgensen et al. (2017) for cluster early-type galaxies in the range $0.2 < z < 0.9$ are shown (green dot-dashed curves). The local relations, age and metallicity versus σ_e and dynamical mass, from Thomas et al. (2010) (dashed curves) are also resported, for sake of completeness. These relations, indeed, cannot be used as direct comparison for our sample, since they have been derived from a sample that includes galaxies at $z \sim 0$ with ages younger than the lookback time ($t_{LB} \sim 8.5$ Gyr) corresponding to $z \sim 1.2$ (especially at the lowest end of our velocity dispersion range), whose progenitors are likely not included in our sample. To overcome this problem, we constructed a local sample of spheroids with properties similar to our sample, from which we derived the local reference relations. We extracted from the SPIDER sample (La Barbera et al. 2010a) at $z \sim 0.07$, a sample of galaxies with $\sigma_e > 190$ km/s (i.e. the range where 6 out of our 7 spheroids lie) and ages older than 7 Gyr.³ The derived relations, age versus σ_e , M_{dyn} and Σ_e , passively evolved back in time, are shown in Fig. 5 as black solid curves. The stellar mass densities Σ_e are derived using Sersic effective radius and stellar masses based on Vazdekis et al. (2010) models and Chabrier IMF (see Swindle et al. 2011).

In each panel, the probability based on the Spearman rank test that the two parameters shown are mutually uncorrelated is also reported. As expected, the relations involving the age and/or the velocity dispersion are those presenting the largest scatters. We do not detect a significant correlation between age and the other parameters of galaxies, such as σ_e , M_{dyn} and Σ_e .

The seven spheroidal galaxies agree with what expected from the extrapolation of the local relations, when they are passively evolved back in time. The data at $z \sim 1.2$ follow the same relations between age and mass, velocity dispersion and mass density, than those at $z \sim 0$. It is worth to note, that the trend of age and metallicity with velocity dispersion may be affected by the aperture within which measurements are done (e.g. La Barbera et al. 2010a; McDermid et al. 2015), because of the presence of metallicity and age gradients both in low-redshift (e.g. Saglia et al. 2000; Wu et al. 2005; La Barbera & de Carvalho 2009; Marian et al. 2018) and in high-redshift spheroids (e.g. Guo et al. 2011; Gargiulo et al. 2011, 2012; Chan et al. 2016; Ciocca et al. 2017). However, it has been shown that measurements within different regions affect the offsets of the relations but not (significantly) their slope (e.g. McDermid et al. 2015; Gargiulo et al. 2017). The agreement of our data with the local relations and with those found by Jørgensen et al. (2017) over the range

³ Notice that we allowed for an age younger than t_{LB} , to account for the progenitor bias, yet leaving room to spheroids that may have experienced a secondary minor burst of star formation at later times.

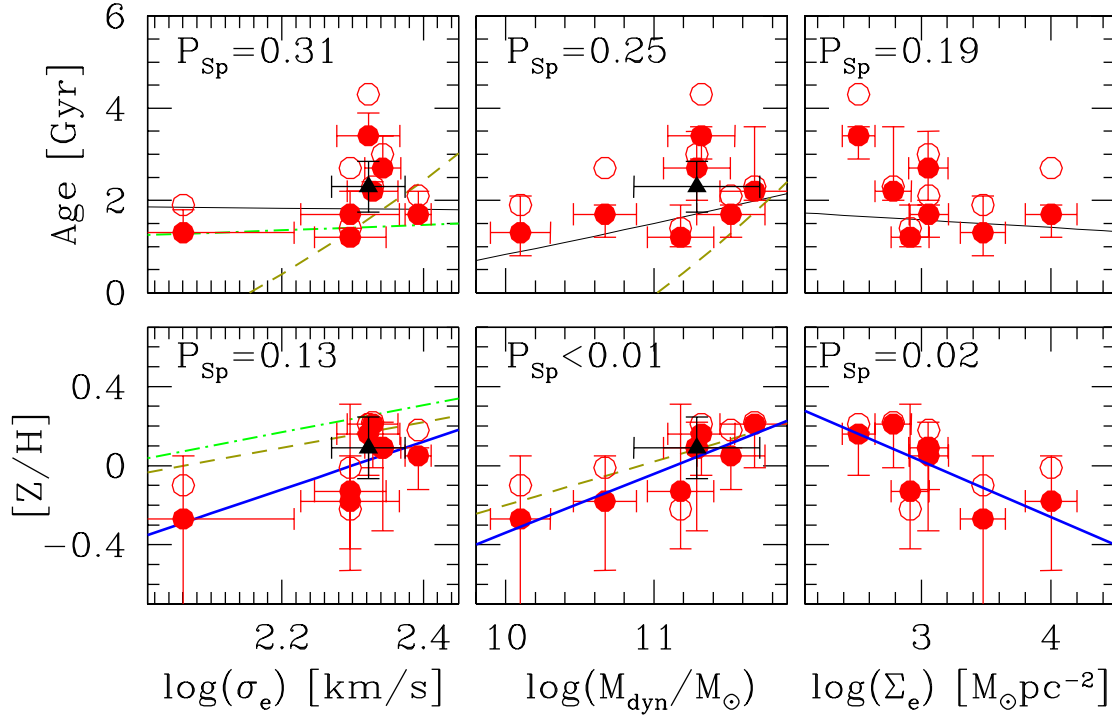


Figure 5. Age (upper panel) and stellar metallicity (lower panel) of galaxies versus velocity dispersion σ_e (left), dynamical mass M_{dyn} (middle) and stellar mass density Σ_e (right). Each panel reports the probability P_{Sp} based on the Spearman rank test that the light-weighted Age and $[Z/H]$ are uncorrelated with each quantity on the x-axis. The red filled (open) circles are the light-weighted (mass-weighted) values obtained for the 7 spheroidal galaxies in the cluster XLSS0223 at $z = 1.22$ (see Tab. 5); the black triangle is the median value. The dark gray dashed curves are the relations of light-weighted Age and $[Z/H]$ with velocity dispersion and dynamical mass found by [Thomas et al. \(2010\)](#) for local galaxies. The black solid curves are the local relations we derived using a sample extracted from the SPIDER sample (see §6; [La Barbera et al. 2010a](#)). These relations are evolved back in time to $z = 1.22$ in the upper panel under the assumption of passive evolution. The green dot-dashed lines are the relations found by [Jørgensen et al. \(2017\)](#) for cluster early-types at $z \sim 0.9$. The thick blue lines in the lower panels are the least-squares fit to the data.

$0.2 < z < 0.9$, confirms this statement and the robustness of the results.

The metallicity $[Z/H]$ of the seven spheroids shows a positive but not statistically significant trend with the velocity dispersion. A least square fit to the data provides the relation

$$[Z/H] = (1.2 \pm 0.5) \log(\sigma_e) - (2.8 \pm 1.2) \quad (5)$$

shown in Fig. 5 (blue solid line), where σ_e [km s $^{-1}$] is the velocity dispersion within the effective radius R_e . The slope agrees with the one found for early-type galaxies in the local universe ([Thomas et al. 2010](#)) and in cluster at $z \sim 0.9$ ([Jørgensen et al. 2017](#)), while the zero point of the relation is offset by about 0.15 dex toward lower metallicity values.

Metallicity is correlated ($\sim 3\sigma$ confidence level, $P_{Sp}=0.006$) with the dynamical mass M_{dyn} . The least square fit to the data provides the relation

$$[Z/H] = (0.29 \pm 0.07) \log(M_{dyn}/M_\odot) - (3.3 \pm 0.8) \quad (6)$$

that agrees well with the local relation of [Thomas et al. \(2010\)](#). Metallicity shows also a negative trend with the stellar mass density Σ_e , with less dense galaxies being more metal rich. These two opposite correlations are due to the anticorrelation between dynamical mass and stellar mass density resulting from the fundamental plane: galaxies with higher total mass are also less dense. This is shown in

Fig. 6 where the dynamical mass is plotted versus the stellar mass density for the seven spheroidal galaxies studied here, belonging to the cluster XLSSJ0223 at $z=1.22$, the early-type galaxies in the cluster RDCSJ0848 at $z = 1.27$, studied by [Jørgensen et al. \(2014\)](#) (samples #4 and #5 of their Tab. 7) and the seven spheroidal galaxies in the cluster XMMJ2235 at $z=1.39$ studied by [Beifiori et al. \(2017\)](#). Two different samples of field spheroidal galaxies in the local universe selected with $\sigma_e > 190$ km s $^{-1}$, are also shown for comparison. The first one, extracted from the sample of [Thomas et al. \(2010\)](#), has stellar mass densities derived using DeVaucouleur effective radii and the stellar masses of [Comparat et al. \(2017\)](#), based on MS11 models ([Maraston & Strömbäck 2011](#)) with Charbier IMF and MILES stellar library. The second one, extracted from the SPIDER sample ([La Barbera et al. 2010a](#)), has stellar mass densities derived using Sersic effective radius and stellar masses based on [Vazdekis et al. \(2010\)](#) models and Chabrier IMF of (see [Swindle et al. 2011](#)). This fundamental relation is shown here for clarity and it will be discussed in detail in a forthcoming paper.

The relationships involving metallicity, dynamical mass and stellar mass density, are rather robust and do not depend either on the models used or on the fitting method. Fig. 7 shows, as example, the relations as obtained through line strengths fitting reported in Tab. 4 (see §4). The same results

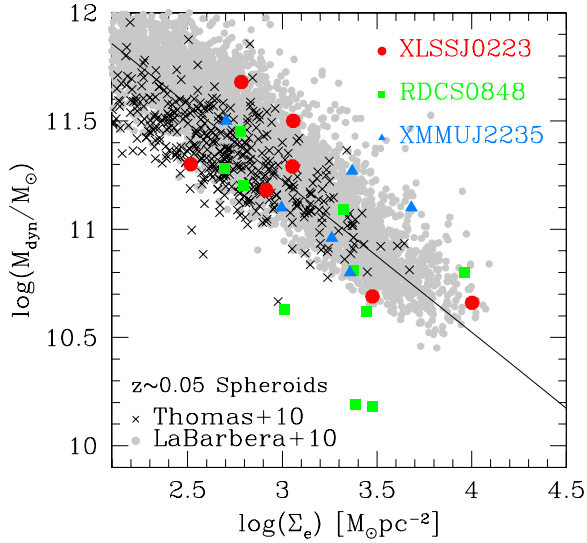


Figure 6. Dynamical mass versus stellar mass density of cluster spheroidal galaxies. The dynamical mass $M_{\text{dyn}} = 5\sigma^2 R_e/G$ of early-type galaxies in clusters at $1.2 < z < 1.4$ is plotted versus their stellar mass density $\Sigma_e = 0.5M^*/\pi R_e^2$. The red filled circles are the 7 spheroidal galaxies in the cluster XLSSJ0223 at $z = 1.22$, the green squares are spheroidal galaxies in the cluster RDCS0848 at $z=1.27$ from Jørgensen et al. (2014), the blue triangles are spheroidal galaxies in the cluster XMMUJ2235 at $z=1.39$ from Beifiori et al. (2017). Black crosses are the spheroidal galaxies at $z \sim 0.05$ with $\sigma_e > 190 \text{ km s}^{-1}$ from the sample of Thomas et al. (2010). Light-gray filled circles are the spheroids at similar redshift with $\sigma_e > 190 \text{ km s}^{-1}$ extracted from the SPIDER sample La Barbera et al. (2010a). The black line represents the orthogonal fit to the high- z cluster data $\log(M_{\text{dyn}}/M_\odot) = (-0.7 \pm 0.2) \log(\Sigma_e) + (13.3 \pm 0.5)$.

are obtained using the parameters obtained with MS11 or BC03 models. Indeed, as shown in Tab. A1 and A2, within each set of results, galaxies keep nearly the same ranking with respect to a given parameter.

The most clear correlation we detect in our data is between metallicity $[Z/H]$ and dynamical mass M_{dyn} . In this case the correlation is statistically significant and becomes much weaker when the velocity dispersion is considered. Overall, we find that the basic trends observed in the local universe, were already established at $z \sim 1.3$: massive spheroids were characterized by higher stellar metallicity, lower mass density and stellar populations tendentially older than the lower mass spheroids. It is worth to recall that, here, the mass is the total mass of the galaxy, includes both dark and baryonic matter.

7 SUMMARY AND CONCLUSIONS

In this paper we have presented an analysis of the stellar populations in seven spheroidal galaxies in the cluster XLSSJ0223 at $z \sim 1.22$. The analysis, based on our optical spectra collected at LBT, is aimed at constraining the epoch of formation and the evolutionary path of these seven spheroids through the derivation of their main stellar popu-

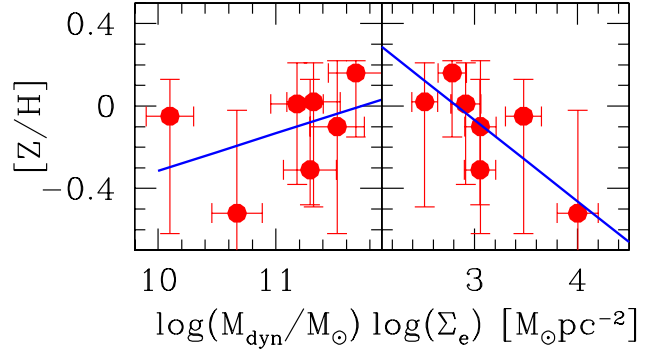


Figure 7. Same as Fig. 5 but for the stellar population parameters of Tab. 4 resulting from the fitting of spectral line indices (see §4).

lation parameters, age and metallicity, and the reconstruction of their SFHs.

We have measured absorption line strengths in the rest-frame 3400-4300 Å and used them to constrain the age and the metallicity of the stellar populations through the comparison with measurements at lower redshift from the literature and predictions from stellar population models. We find that the metallicity of these spheroids is not different from the metallicity measured in early-type galaxies in clusters at lower redshift.

We then derived the age and the metallicity of the stellar populations from spectral fitting. The resulting median metallicity of the seven galaxies is $[Z/H] = 0.09 \pm 0.16$, with all the values within 0.2 dex from the solar value. These values agree with those of early-type galaxies in clusters at $0 < z < 0.9$ and with the few single measurements of field early-types at higher redshift. The constant metallicity value over the redshift range $0 < z < 1.3$ shows that no significant metallicity evolution for the population of cluster early-types has taken place over the last 9 billion years. This implies also that no significant additional star formation and chemical enrichment are required for these seven spheroids to join the present-day population of cluster early-type galaxies.

The median mass-weighted age of the seven spheroids is $\langle \text{Age}_M \rangle = 2.4 \pm 0.6 \text{ Gyr}$, corresponding to a formation redshift $\langle z_f \rangle \sim 2.6^{+0.7}_{-0.5}$, or a median Lookback Time = $11^{+0.6}_{-1.0} \text{ Gyr}$. We find a significant scatter in galaxy ages and, consequently, in formation redshifts, showing that the population of massive spheroids, at least in the cluster XLSSJ0223, is not coeval. On the other hand, galaxy ages agree with those measured for cluster early-types at lower redshift and passive evolution would lead our sample to join the present-day population.

We compared the relations between age and metallicity with velocity dispersion and dynamical mass of the seven spheroids with those at lower redshift and in the local universe. We do not detect any significant correlation between age and the structural parameters considered, velocity dispersion σ_e , dynamical mass M_{dyn} and effective stellar mass density Σ_e . This is possibly because of the large intrinsic scatter of the age of a stellar population, which is affected by many physical/local parameters, and the small number of galaxies. The age-velocity dispersion, age-mass and age-

mass density relations of the seven spheroids agree with those derived for local spheroids, once passively evolved back in time and progenitor bias is taken into account.

On the contrary, we find that the metallicity $[Z/H]$ is correlated to dynamical mass M_{dyn} , according to a relation very similar to the one obtained for local spheroidal galaxies. We also show that the metallicity $[Z/H]$ is anticorrelated to the stellar mass density Σ_e because of the anticorrelation between M_{dyn} and Σ_e .

The data show that no significant metallicity evolution for the population of cluster galaxies has taken place in the last 9 billion years. This suggests that no additional major episodes of star formation/chemical enrichment or minor mergers (that would dilute the metallicity) are experienced by cluster spheroidal galaxies at $z \sim 1.3$ to join the local population.

We find that the basic trends observed in the local universe, were already established at $z \sim 1.3$, with more massive spheroids having higher metallicity, lower stellar mass density and older ages than their lower mass counterparts.

ACKNOWLEDGEMENTS

We thank the referee for the usefull and constructive comments that improved the presentation of the results. This work is based on observations carried out at the Large Binocular Telescope (LBT) under program ID 2015_2016_28. The LBT is an international collaboration among institutions in the US, Italy and Germany. We acknowledge the support from the LBT-Italian Coordination Facility for the execution of the observations, the data distribution and for support in data reduction. We thank D. Thomas and J. Lian for having provided us with the median metallicity values of eBOSS galaxies from Comparat et al. (2017). PS would like to thank T. Durden for the useful suggestions.

REFERENCES

- Andreon S., Valtchanov I., Jones L. R., Altieri B., Bremer M., Willis J., Pierre M., Quintana H., 2005, *MNRAS*, 359, 1250
- Asari N. V., Cid Fernandes R., Stasińska G., Torres-Papaqui J. P., Mateus A., Sodré L., Schoenell W., Gomes J. M., 2007, *MNRAS*, 381, 263
- Balogh M. L., Morris S. L., Yee H. K. C., Carlberg R. G., Ellingson E., 1999, *ApJ*, 527, 54
- Beifiori A., Maraston C., Thomas D., Johansson J., 2011, *A&A*, 531, A109
- Beifiori A., et al., 2017, *ApJ*, 846, 120
- Belli S., et al., 2017, *ApJ*, 841, L6
- Bender R., Burstein D., Faber S. M., 1993, *ApJ*, 411, 153
- Bernardi M., 2009, *MNRAS*, 395, 1491
- Bernardi M., et al., 2003, *AJ*, 125, 1866
- Bernardi M., Nichol R. C., Sheth R. K., Miller C. J., Brinkmann J., 2006, *AJ*, 131, 1288
- Bremer M. N., et al., 2006, *MNRAS*, 371, 1427
- Brooks A., Christensen C., 2016, in Laurikainen E., Peletier R., Gadotti D., eds, *Astrophysics and Space Science Library* Vol. 418, *Galactic Bulges*. p. 317 ([arXiv:1511.04095](https://arxiv.org/abs/1511.04095)), doi:10.1007/978-3-319-19378-6_12
- Bruzual A. G., 1983, *ApJS*, 53, 497
- Bruzual G., Charlot S., 2003, *MNRAS*, 344, 1000
- Buzzoni A., Gariboldi G., Mantegazza L., 1992, *AJ*, 103, 1814
- Calzetti D., Armus L., Bohlin R. C., Kinney A. L., Koornneef J., Storchi-Bergmann T., 2000, *ApJ*, 533, 682
- Cappellari M., 2017, *MNRAS*, 466, 798
- Cappellari M., Emsellem E., 2004, *PASP*, 116, 138
- Cardelli J. A., Clayton G. C., Mathis J. S., 1989, *ApJ*, 345, 245
- Carollo C. M., et al., 2013, *ApJ*, 773, 112
- Chabrier G., 2003, *PASP*, 115, 763
- Chan J. C. C., et al., 2016, *MNRAS*, 458, 3181
- Cid Fernandes R., Mateus A., Sodré L., Stasińska G., Gomes J. M., 2005, *MNRAS*, 358, 363
- Cid Fernandes R., Asari N. V., Sodré L., Stasińska G., Mateus A., Torres-Papaqui J. P., Schoenell W., 2007, *MNRAS*, 375, L16
- Cimatti A., et al., 2008, *A&SA*, 482, 21
- Ciocca F., Saracco P., Gargiulo A., De Propriis R., 2017, *MNRAS*, 466, 4492
- Ciotti L., Lanzoni B., Volonteri M., 2007, *ApJ*, 658, 65
- Colless M., Burstein D., Davies R. L., McMahan R. K., Saglia R. P., Wegner G., 1999, *MNRAS*, 303, 813
- Comparat J., et al., 2017, preprint ([arXiv:1711.06575](https://arxiv.org/abs/1711.06575))
- Cooper M. C., Tremonti C. A., Newman J. A., Zabludoff A. I., 2008, *MNRAS*, 390, 245
- Davidge T. J., Clark C. C., 1994, *AJ*, 107, 946
- Falcón-Barroso J., Sánchez-Blázquez P., Vazdekis A., Ricciardelli E., Cardiel N., Cenarro A. J., Gorgas J., Peletier R. F., 2011, *A&A*, 532, A95
- Ferreras I., et al., 2018, preprint ([arXiv:1805.03665](https://arxiv.org/abs/1805.03665))
- Fisher D., Franx M., Illingworth G., 1995, *ApJ*, 448, 119
- Fukugita M., Nakamura O., Turner E. L., Helmboldt J., Nichol R. C., 2004, *ApJ*, 601, L127
- Gallazzi A., Charlot S., Brinchmann J., White S. D. M., Tremonti C. A., 2005, *MNRAS*, 362, 41
- Gallazzi A., Bell E. F., Zibetti S., Brinchmann J., Kelson D. D., 2014, *ApJ*, 788, 72
- Gargiulo A., Saracco P., Longhetti M., 2011, *MNRAS*, 412, 1804
- Gargiulo A., Saracco P., Longhetti M., La Barbera F., Tamburri S., 2012, *MNRAS*, 425, 2698
- Gargiulo A., Saracco P., Tamburri S., Lonoce I., Ciocca F., 2016, *A&A*, 592, A132
- Gargiulo A., et al., 2017, *A&A*, 606, A113
- George K., 2017, *A&A*, 598, A45
- Gilli R., Vignali C., Mignoli M., Iwasawa K., Comastri A., Zamorani G., 2010, *A&A*, 519, A92
- Girardi L., Bressan A., Bertelli G., Chiosi C., 2000, *A&AS*, 141, 371
- Gorgas J., Cardiel N., Pedraz S., González J. J., 1999, *A&AS*, 139, 29
- Greggio L., 1997, *MNRAS*, 285, 151
- Greggio L., Renzini A., 2011, *Stellar Populations. A User Guide from Low to High Redshift*
- Guo Y., et al., 2011, *ApJ*, 735, 18
- Haehnelt M. G., Madau P., Kudritzki R., Haardt F., 2001, *ApJ*, 549, L151
- Harrison C. D., Colless M., Kuntschner H., Couch W. J., de Propriis R., Pracy M. B., 2011, *MNRAS*, 413, 1036
- Huang S., Gu Q.-S., 2009, *MNRAS*, 398, 1651
- Jørgensen I., 1999, *MNRAS*, 306, 607
- Jørgensen I., Chiboucas K., 2013, *AJ*, 145, 77
- Jørgensen I., Chiboucas K., Toft S., Bergmann M., Zirm A., Schiavon R. P., Grützbauch R., 2014, *aj*, 148, 117
- Jørgensen I., Chiboucas K., Berkson E., Smith O., Takamiya M., Villaume A., 2017, *AJ*, 154, 251
- Kausch W., et al., 2015, *A&A*, 576, A78
- Kennicutt Jr. R. C., 1998, *ARA&A*, 36, 189
- Kriek M., et al., 2016, *Nature*, 540, 248
- La Barbera F., de Carvalho R. R., 2009, *ApJ*, 699, L76
- La Barbera F., de Carvalho R. R., de La Rosa I. G., Lopes P. A. A., Kohl-Moreira J. L., Capelato H. V., 2010a, *MNRAS*,

408, 1313
 La Barbera F., de Carvalho R. R., de La Rosa I. G., Lopes P. A. A., 2010b, *MNRAS*, 408, 1335
 La Barbera F., Lopes P. A. A., de Carvalho R. R., de La Rosa I. G., Berlind A. A., 2010c, *MNRAS*, 408, 1361
 Longhetti M., Bressan A., Chiosi C., Rampazzo R., 1999, *A&A*, 345, 419
 Lonoce I., Longhetti M., Saracco P., Gargiulo A., Tamburri S., 2014, *MNRAS*, 444, 2048
 Lonoce I., et al., 2015, *MNRAS*, 454, 3912
 Maraston C., Strömbäck G., 2011, *MNRAS*, 418, 2785
 Marian V., Ziegler B., Kuchner U., Verdugo M., 2018, preprint ([arXiv:1806.10625](https://arxiv.org/abs/1806.10625))
 Mateus A., Sodr   L., Cid Fernandes R., Stasi  nska G., 2007, *MNRAS*, 374, 1457
 McDermid R. M., et al., 2015, *MNRAS*, 448, 3484
 Morishita T., et al., 2018, *ApJ*, 856, L4
 Munari U., Sordo R., Castelli F., Zwitter T., 2005, *A&A*, 442, 1127
 Naab T., Johansson P. H., Ostriker J. P., Efstathiou G., 2007, *ApJ*, 658, 710
 Onodera M., et al., 2015, *ApJ*, 808, 161
 Oser L., Naab T., Ostriker J. P., Johansson P. H., 2012, *ApJ*, 744, 63
 Pickles A. J., 1985, *ApJS*, 59, 33
 Pietrinferni A., Cassisi S., Salaris M., Castelli F., 2004, *ApJ*, 612, 168
 Pogge R. W., et al., 2010, in *Ground-based and Airborne Instrumentation for Astronomy III*. p. 77350A
 Porter L. A., Somerville R. S., Primack J. R., Johansson P. H., 2014, *MNRAS*, 444, 942
 Rose J. A., 1994, *AJ*, 107, 206
 Rose J. A., Bower R. G., Caldwell N., Ellis R. S., Sharples R. M., Teague P., 1994, *AJ*, 108, 2054
 Saglia R. P., Maraston C., Greggio L., Bender R., Ziegler B., 2000, *A&A*, 360, 911
 S  nchez-Bl  zquez P., et al., 2006, *MNRAS*, 371, 703
 Saracco P., Gargiulo A., Ciocca F., Marchesini D., 2017, *A&A*, 597, A122
 Schmidt M., et al., 1998, *A&A*, 329, 495
 Swindle R., Gal R. R., La Barbera F., de Carvalho R. R., 2011, *AJ*, 142, 118
 Thomas D., Maraston C., Bender R., Mendes de Oliveira C., 2005, *ApJ*, 621, 673
 Thomas D., Maraston C., Schawinski K., Sarzi M., Silk J., 2010, *MNRAS*, 404, 1775
 Trager S. C., Worthey G., Faber S. M., Burstein D., Gonz  lez J. J., 1998, *ApJS*, 116, 1
 Trager S. C., Faber S. M., Worthey G., Gonz  lez J. J., 2000, *AJ*, 120, 165
 Treu T., Ellis R. S., Kneib J.-P., Dressler A., Smail I., Czoske O., Oemler A., Natarajan P., 2003, *ApJ*, 591, 53
 Valdes F., Gupta R., Rose J. A., Singh H. P., Bell D. J., 2004, *ApJS*, 152, 251
 Vazdekis A., S  nchez-Bl  zquez P., Falc  n-Barroso J., Cenarro A. J., Beasley M. A., Cardiel N., Gorgas J., Peletier R. F., 2010, *MNRAS*, 404, 1639
 Woodrum C., J  rgensen I., Fisher R. S., Oberhelman L., Demarco R., Contreras T., Bieker J., 2017, *ApJ*, 847, 20
 Worthey G., Ottaviani D. L., 1997, *ApJS*, 111, 377
 Wu H., Shao Z., Mo H. J., Xia X., Deng Z., 2005, *ApJ*, 622, 244
 Yates R. M., Kauffmann G., 2014, *MNRAS*, 439, 3817
 de La Rosa I. G., La Barbera F., Ferreras I., de Carvalho R. R., 2011, *MNRAS*, 418, L74
 van Dokkum P. G., Franx M., 2001, *ApJ*, 553, 90

Table A1. Age and metallicity estimates resulting from spectral fitting with **STARLIGHT** using BC03 SSP models.

| ID | Age _L [Gyr] | [Z/H] _L | Age _{M*} [Gyr] | [Z/H] _{M*} |
|------|---------------------------|--------------------|----------------------------|---------------------|
| 651 | 2.6 | +0.10 | 2.8 | +0.19 |
| 972 | 3.2 | +0.12 | 4.0 | +0.19 |
| 1142 | 3.0 | +0.15 | 3.6 | +0.16 |
| 1370 | 2.6 | -0.40 | 3.0 | -0.21 |
| 1442 | 1.7 | -0.13 | 2.7 | +0.01 |
| 1630 | 1.0 | +0.17 | 1.3 | +0.05 |
| 1711 | 1.2 | 0.35 | 1.9 | 0.40 |

Table A2. Same as Tab. A1 but for MS11 SSP models.

| ID | Age _L [Gyr] | [Z/H] _L | Age _{M*} [Gyr] | [Z/H] _{M*} |
|------|---------------------------|--------------------|----------------------------|---------------------|
| 651 | 2.2 | +0.05 | – | – |
| 972 | 2.5 | +0.30 | – | – |
| 1142 | 2.0 | +0.30 | – | – |
| 1370 | 2.6 | -0.00 | – | – |
| 1442 | 1.7 | -0.01 | – | – |
| 1630 | 0.7 | +0.13 | – | – |
| 1711 | 1.2 | 0.22 | – | – |

APPENDIX A: RESULTS OF SPECTRAL FITTING WITH DIFFERENT MODELS

In this appendix we report the result of the spectral fitting performed with **STARLIGHT** using a set of BC03 SSPs (Bruzual & Charlot 2003) and a set of MS11 SSPs (Maraston & Str  mb  ck 2011). Both the sets of models are based on Chabrier IMF. For the BC03 models, we considered 20 ages in the range [0.06; 4.5] Gyr and 5 metallicities in the range [-1.7; 0.4], the results are shown in Tab. A1. For MS11 models we considered 20 ages in the range [0.06; 4.5] Gyr and 5 metallicities in the range [-2.3; 0.3], the results are shown in Tab. A2.

We emphasize that the ranking of galaxies with respect to each parameter (either age or metallicity), is very similar for both sets of stellar population models (see also   5), confirming the robustness of our results.

This paper has been typeset from a T  X/L  T  X file prepared by the author.